Validation of linearity assumptions for using tsunami waveforms in joint inversion of kinematic rupture models: Application to the 2010 Mentawai M_w 7.8 tsunami earthquake

Han Yue[1,2], Thorne Lay[1], Linyan Li[3], Yoshiki Yamazaki[3], Kwok Fai Cheung[3], Luis Rivera[4], Emma M. Hill[5], Kerry Sieh[5], Widjo Kongko[6], and Abdul Muhari[7]

[1]Department of Earth and Planetary Sciences, University of California, Santa Cruz, California, USA, [2]Seismological Laboratory, Division of Geological and Planetary Sciences, California Institute of Technology, Pasadena, California, USA, [3]Department of Ocean and Resources Engineering, University of Hawai'i at Mānoa, Honolulu, Hawaii, USA, [4]Institut de Physique du Globe de Strasbourg, Université de Strasbourg/CNRS, Strasbourg, France, [5]Earth Observatory of Singapore, Nanyang Technological University, Singapore, Singapore, [6]Coastal Dynamic Research Center, Indonesian Agency for the Assessment and Application of Technology, Jogjakarta, Indonesia, [7]International Research Institute of Disaster Science, Tohoku University, Sendai, Japan

Abstract Tsunami observations have particular importance for resolving shallow offshore slip in finite-fault rupture model inversions for large subduction zone earthquakes. However, validations of amplitude linearity and choice of subfault discretization of tsunami Green's functions are essential when inverting tsunami waveforms. We explore such validations using four tsunami recordings of the 25 October 2010 Mentawai M_w 7.8 tsunami earthquake, jointly inverted with teleseismic body waves and 1 Hz GPS (high-rate GPS) observations. The tsunami observations include near-field and far-field deep water recordings, as well as coastal and island tide gauge recordings. A nonlinear, dispersive modeling code, NEOWAVE, is used to construct tsunami Green's functions from seafloor excitation for the linear inversions, along with performing full-scale calculations of the tsunami for the inverted models. We explore linearity and finiteness effects with respect to slip magnitude, variable rake determination, and subfault dimensions. The linearity assumption is generally robust for the deep water recordings, and wave dispersion from seafloor excitation is important for accurate description of near-field Green's functions. Breakdown of linearity produces substantial misfits for short-wavelength signals in tide gauge recordings with large wave heights. Including the tsunami observations in joint inversions provides improved resolution of near-trench slip compared with inversions of only seismic and geodetic data. Two rupture models, with fine-grid (15 km) and coarse-grid (30 km) spacing, are inverted for the Mentawai event. Stronger regularization is required for the fine model representation. Both models indicate a shallow concentration of large slip near the trench with peak slip of ~15 m. Fully nonlinear forward modeling of tsunami waveforms confirms the validity of these two models for matching the tsunami recordings along with the other data.

1. Introduction

During the last few decades, geophysicists have accumulated extensive observations of signals produced by large earthquakes from greatly expanded seismic, geodetic, tsunami, and gravity recording systems. Models of space-time fault slip distributions inverted from these data sets reveal the complexity of large ruptures and guide our understanding of fault friction and stress heterogeneity [e.g., *Kanamori*, 2014; *Lay*, 2014]. Obtaining robust finite-fault rupture models remains challenging due to intrinsic limitations of each signal type, which motivates joint inversions of all observations to exploit their complementary advantages and to reduce nonuniqueness.

Seismic data have been used for finite-fault model inversions since the 1980s [e.g., *Hartzell and Heaton*, 1983; *Kikuchi and Kanamori*, 1991; *Kikuchi et al.*, 1993; *Ji et al.*, 2002], with the global density and distribution of broadband seismic recordings rapidly expanding after 1990. Teleseismic body waves provide good temporal resolution of the moment rate function, while longer-period surface waves provide good resolution of the total seismic moment. The National Earthquake Information Center now routinely inverts global seismic wave data for finite-fault models for many $M_w \geq 7.0$ earthquakes. However, due to large trade-offs between time

and location of slip, teleseismic data still have limited spatial resolution of the slip distribution in finite-fault models [e.g., *Lay et al.*, 2010]. Kinematic rupture model inversions from teleseismic data sets can always benefit from independent constraints on the rupture finiteness.

GPS and interferometric synthetic aperture radar (InSAR) techniques have been developed and applied to investigate coseismic rupture patterns since the 1990s [e.g., *Goldstein et al.*, 1993; *Massonnet et al.*, 1993; *Freymueller et al.*, 1994; *Bürgmann et al.*, 2000; *Simons and Rosen*, 2007]. For inland earthquakes, especially in arid areas, geodetic observations from InSAR, campaign GPS, Landsat, and other high-resolution imaging systems can provide dense sampling of coseismic surface deformation, resolving finite-fault static offsets with high spatial resolution [e.g., *Shen et al.*, 2009; *Tong et al.*, 2010; *Avouac et al.*, 2014]. However, for most megathrust and oceanic events, geodetic observations do not cover the rupture area sufficiently to fully resolve the offshore rupture pattern. When only on-land static deformation observations are available, a priori constraints are usually applied to stabilize slip estimates near the trench [e.g., *Pollitz et al.*, 2011]. High-rate GPS (hr-GPS) observations with ground motion solutions at 1 s sampling combine the advantages of both seismic and campaign geodetic observations by capturing both the time-varying and static deformation fields, yielding finite-fault models with improved spatial and temporal resolution [e.g., *Miyazaki et al.*, 2004; *Yue and Lay*, 2011, 2013]. The resolution far offshore is still limited in hr-GPS inversions due to the weak signal excitation by slip near the trench. In almost all seismic and geodetic inversions using only onshore data, the near-trench slip distribution remains hard to constrain.

Tsunami-based finite-fault models were first developed in the 1980s [e.g., *Satake*, 1987, 1989, 1993; *Johnson et al.*, 1996], initially relying on complicated tide gauge recordings in harbors (usually analog records) and more recently using signals from deep water ocean bottom pressure gauges that are much more robust for source investigations [e.g., *Saito et al.*, 2011; *Satake et al.*, 2013a; *An et al.*, 2014]. Shallow near-trench slip is a strong source for tsunami waves because it produces large seafloor displacements in the deepest part of the surrounding ocean, making tsunami the most sensitive wave type for constraining rupture near the toe of sedimentary wedges [e.g., *Lorito et al.*, 2011; *Satake et al.*, 2013a; *Lay et al.*, 2014; *Yue et al.*, 2014b]. The low-propagation velocities of tsunami further provide intrinsically good spatial resolution of offshore source finiteness. There are significant limitations of tsunami-only inversions; tsunami observations involve low-frequency signals, with limited temporal resolution [*Satake et al.*, 2013a], limited resolution of fine-scale rupture patterns [*Yue et al.*, 2014a], and a strong dependence on the accuracy of available bathymetry information. Approximations commonly made in computing tsunami wave propagation can lead to errors in arrival times that limit the resolution of slip distribution. Also, tsunami waves are not very sensitive to deeper slip on the fault if rupture extends under land [e.g., *Yue et al.*, 2014b], so it is most useful to combine them with other data types.

Joint inversions with different signal types strive to exploit the useful information of each data set by fitting them simultaneously, giving rupture models with improved spatial, temporal, and moment resolution [e.g., *Satake*, 1993; *Romano et al.*, 2010, 2012, 2014; *Lorito et al.*, 2011; *Yokota et al.*, 2011; *Lay et al.*, 2014; *Yue and Lay*, 2013; *Yue et al.*, 2014b; *Bletery et al.*, 2014]. Most kinematic rupture inversions explicitly utilize linear techniques, which assume proportionality of Green's functions with slip and utilize superposition of the subfault contributions in the model. For linear elasticity theory, these linearity assumptions hold well for seismic and geodetic signals, introducing no theoretical complexity when inverting seismic and geodetic data jointly other than ensuring a fault model parameterization compatible with the seismic signal frequency content. For tsunami waves, the linear assumption of scaling with slip is theoretically valid as long as the wave amplitude is much smaller than the water depth. Therefore, it generally holds for deep ocean tsunami waves, where wave amplitude (meters) is much smaller than the water depth (kilometers). However, the linear assumption breaks down for shallow-water recordings if tsunami wave amplitude is larger than ~10% of the water depth (e.g., near coastal areas or islands). This can be demonstrated by comparison of results for varying slip magnitudes computed with a fully nonlinear code. Linearity with respect to model discretization and finiteness effects is also an issue for tsunami inversions, given that subfault dimensions affect the periods of tsunami excitation and integration over the finite fault must be shown to give stable broadband waveforms relative to superposition of subfault responses.

In addition to assuming linearity, commonly used inversion routines make use of tsunami Green's functions generated by nondispersive hydrostatic models. A common assumption is that the initial sea surface elevation is identical to the seafloor vertical displacement, and the resulting waves propagate at the shallow-water
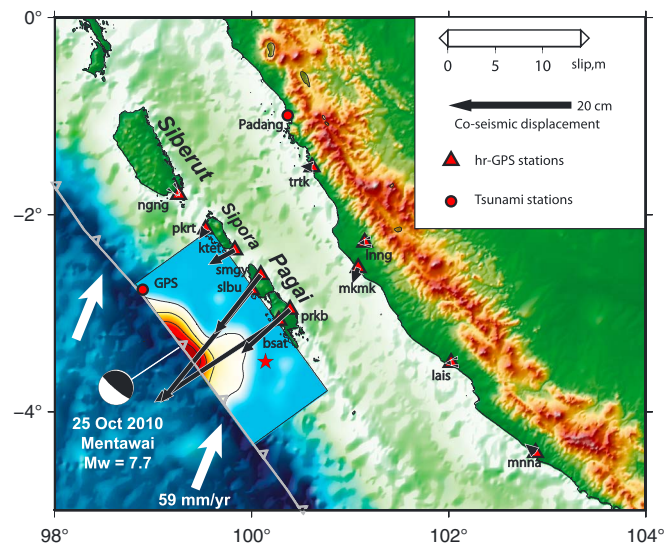
Figure 1. Map of the study area. The epicenter of the 25 October 2010 M_w 7.8 Mentawai event is marked with a red-filled star. The global centroid-moment tensor solution is shown by the black-filled focal mechanism. The coseismic rupture pattern found in this paper is indicated with a blue/red color scale. The trench is marked with barbed gray curve. The hr-GPS stations used in the joint inversion are indicated with red-filled triangles with black arrows showing coseismic horizontal static displacement vectors. Two tsunami stations near the source region, the GPS buoy and Padang, are marked with red-filled circles. Larger Mentawai Islands are labeled. Plate motion direction of the Australian plate relative to a fixed Sunda plate is indicated with white arrows.

celerity independent of the wavelength. Use of subfaults with modest dimensions relative to water depth requires calculation of tsunami excitation using seafloor displacement rather than static sea surface displacements [e.g., *Kaijura*, 1963] to account for attenuation of vertical displacements across the water column. These dispersion effects in tsunami generation give rise to maximum sea surface elevation that is only a fraction of the seafloor vertical displacement. The shorter-period waves in the initial pulse tend to propagate at lower speeds resulting in a sequence of waves with reduced initial peak amplitude. These effects must be additive or subtractive in an inversion routine to reproduce both long-period nondispersive and short-period dispersive waves from a wide range of rupture size. Given the concerns about linearity and dispersion of tsunami waves, our previous work has emphasized fully nonlinear and weakly dispersive forward modeling of tsunami signals predicted by seismic and geodetic inversion models, iteratively searching extensively (and tediously) over model parameters to find optimal finite-fault models compatible with tsunami, seismic, and geodetic observations [e.g., *Lay et al.*, 2011a, 2011b, 2013a, 2013b; *Yamazaki et al.*, 2011b; *Yue et al.*, 2014a; *Bai et al.*, 2014]. In particular, *Lay et al.* [2013a, 2013b] showed significant effects of dispersion in the generation and propagation of the tsunami resulting from the 2013 Santa Cruz Islands and the 2012 Haida Gwaii earthquakes.

The recent joint inversion studies of the 2011 Tohoku earthquake and tsunami by *Romano et al.* [2012, 2014] and *Bletery et al.* [2014] have calculated tsunami Green's functions using the fully nonlinear, nonhydrostatic model NEOWAVE from *Yamazaki et al.* [2009, 2011a]. This code has undergone thorough benchmarking by the National Tsunami Hazard Mitigation Program, as discussed in *Yamazaki et al.* [2012]. The capability to account for tsunami excitation by seafloor displacement and wave dispersion during the generation process facilitates effective use of tsunami measurements around the source and deduction of the large and narrow slip zone near the trench by the inversion routines. A systematic assessment of the linearity and dispersion properties will help verify and validate the approach for general application. In this paper, we build on our prior iterative inversion and nonhydrostatic modeling study of the 25 October 2010 Mentawai M_w 7.8 tsunami earthquake [*Yue et al.*, 2014a, henceforth identified as Paper 1], directly incorporating tsunami observations together with hr-GPS and teleseismic body wave signals in joint linear inversions. We explore the joint inversions for this well-studied earthquake to validate the linear assumptions about the Green's functions for deep water and tide gauge tsunami observations, while also refining the rupture model for this important megathrust earthquake.

2. The 2010 M_w 7.8 Mentawai Tsunami Earthquake

The 25 October 2010 M_w 7.8 thrust earthquake (14:42:21.4 UTC, 3.49°S, 100.14°E, Badan Meteorologi, Klimatologi dan Geofisika (BMKG)) ruptured the shallow portion of the Sunda megathrust seaward of the Pagai Islands (Figure 1). The coseismic rupture process of the 2010 Mentawai earthquake has been investigated using various combinations of seismic, geodetic, and tsunami observations [*Bilek et al.*, 2011;

Lay et al., 2011a; *Newman et al.*, 2011; *Hill et al.*, 2012; *Satake et al.*, 2013b; Paper 1]. Seismic wave investigations [*Bilek et al.*, 2011; *Lay et al.*, 2011a; *Newman et al.*, 2011] resolved an overall northwestward rupture propagation with a low rupture velocity of ~1.5 km/s and a long source duration exceeding 110 s. Localized maximum slip exceeding 4 m near the trench was found in a model by *Lay et al.* [2011a], and this was shown to be consistent with a deep water tsunami observation at a distant DART station, but the spatial resolution was limited. *Hill et al.* [2012] analyzed regional GPS observations from the Sumatra GPS Array (SuGAr) network (Figure 1) and, based on reconciling both the GPS and tsunami field observations, favored a narrow patch with ~12 m of slip extending 120 km along the shallow fault zone. *Satake et al.* [2013b] inverted tsunami waves observed at 11 tsunami sites and performed forward modeling to compare with inundation surveys, finding two localized slip patches with 4–6 m of peak slip near the trench. Resolution of slip near the toe of the prism is important for evaluating strain accumulation and frictional properties of the shallow megathrust. Conventional assumptions of velocity-strengthening friction with stable sliding for shallow sediments [e.g., *Scholz*, 1998] are inconsistent with large unstable slip at very shallow depth, yet it clearly occurs locally. This may be due to local frictional anomalies associated with subducted seamounts or other bathymetry, or it may be a manifestation of conditional stability for which accelerated strain rate drives friction into instability.

Paper 1 combined SuGAr hr-GPS and teleseismic observations in joint kinematic inversions and iteratively performed forward modeling to fit several tsunami observations, adjusting fault dimensions, rupture velocity, and subfault source time functions to achieve satisfactory fits to all the data. A rupture model with two significant rupture concentrations near the trench was found in Paper 1, with the maximum slip being much higher (>20 m) than in other studies. Although key inversion parameters were tested and optimized for the tsunami data in this iterative modeling approach, the rupture pattern is actually constrained by the assumed kinematic parameters and regularization, not directly by the tsunami data. While good fits were achieved after a number of iterations, artifacts may have been introduced by the forward modeling approach.

Here we directly include the tsunami observations in joint inversions to objectively utilize the full information in the tsunami waves. However, this approach immediately raises issues of linearity of the tsunami modeling [e.g., *Melgar and Bock*, 2013], and these are thus carefully considered.

3. Tsunami Observations and Green's Function Linearity

3.1. Tsunami Observations of the Mentawai Earthquake

The tsunami observations used here for the 2010 Mentawai event are the same data that were iteratively forward modeled in Paper 1. This includes two deep water recordings (from GITEWS GPS 03 and DART 56001; Figure 2) and two tide gauge observations (from Cocos Island and Padang Bay; Figure 2). In this section, general issues of linearity for modeling these observations are considered.

The tsunami recorded at DART 56001, 1600 km from the epicenter, had relatively simple propagation effects and was recorded in deep water, so the waves are dominated by long-wavelength pulses followed by dispersed and scattered coda. The main pulse provides integral constraints on the source slip distribution, but not spatial details of the slip, as found in earlier studies [*Hill et al.*, 2012; *Satake et al.*, 2013b; Paper 1]. The GPS buoy observations are unusual in being very close to the rupture area (Figure 1), and while they are also in deep water, the signals contain short-period near-field waves that are quite sensitive to the slip distribution and its timing. The tsunami recorded by the Padang tide gauge station traveled through the shallow passages between the Mentawai islands (Figure 2b), where the waves were refracted and diffracted. The coda waves in the Padang data include multiple short-wavelength reflected waves behind headlands (Figure 2c), which may be influenced by nonlinearity of the shallow water of less than 8 m depth in the bay (Figure 2d). The Cocos Island tide gauge recorded even more complex waves in a lagoon of ~12 km diameter and 2 to 5 m deep atop an atoll. The coda lasts 4 to 6 times longer than the initial peak due to "ringing" of waves trapped by the island and an adjacent atoll (Figures 2e and 2f). These four tsunami records sample different propagation characteristics and have varying sensitivity to the slip space-time history, which allows us to examine various linearization issues.

3.2. Fault Model Parameterizations

To test the linearity of tsunami wave superposition and to calculate tsunami Green's functions for the linear inversions discussed below, we parameterized both "fine-grid" and "coarse-grid" representations of the fault
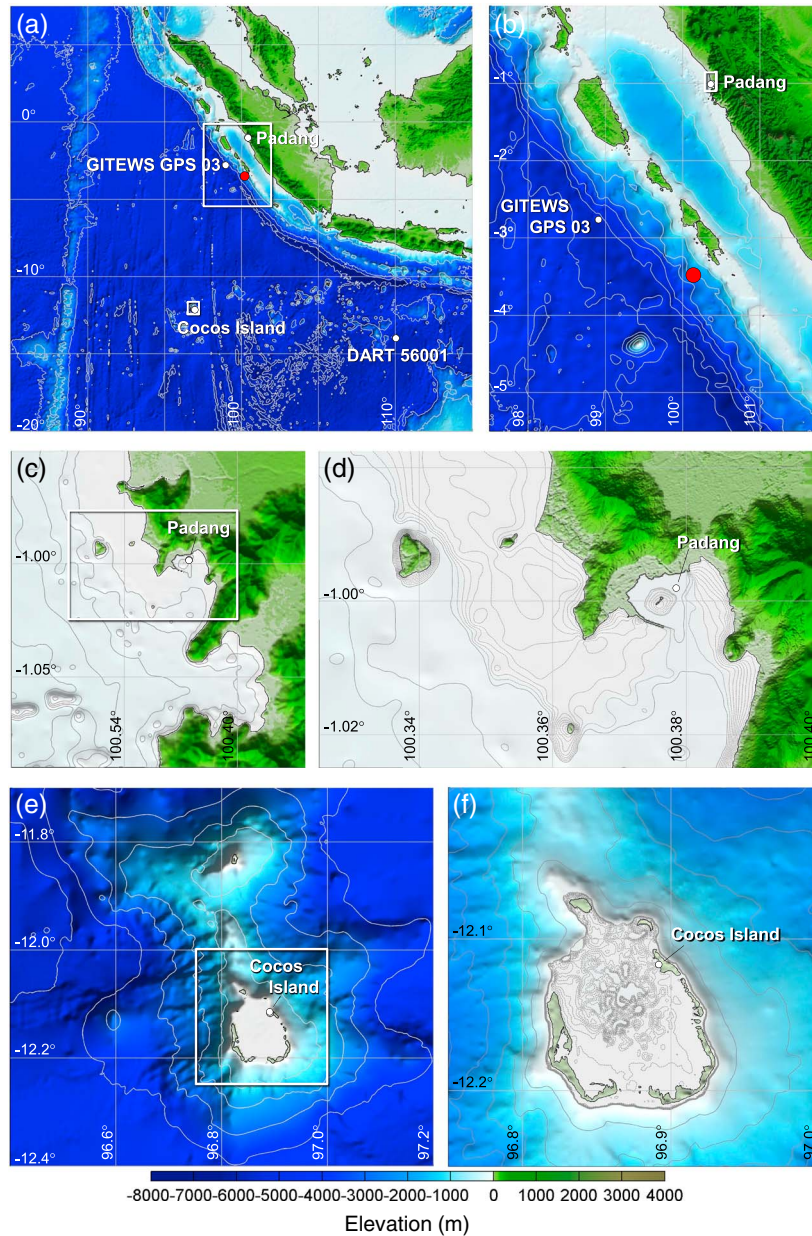
Figure 2. Location map and nested grid system for modeling of the 25 October 2010 Mentawai earthquake tsunami. (a) Level 1 grid over northeast Indian Ocean with the outlines of the level 2 grids over the near-field and Cocos Island regions. Grey solid lines indicate the depth contours at 2000 m intervals. (b) Level 2 grid of the near-field region with the outline of the level 3 grid over the Padang coastal region. Grey solid lines indicate depth contours at 1000 m intervals. White circles indicate water level stations and red circle indicates the epicenter. (c) Level 3 grid of the Padang coastal region with the outline of the level 4 grid at Padang Harbor. Grey solid lines indicate depth contours at 10 m intervals. (d) Level 4 grid at Padang Harbor. Grey solid lines indicate depth contours at 10 m intervals and grey dot lines indicate depth contours at 1 m intervals. (e) Level 2 grid of the Cocos Island region with the outline of the level 3 grid over Cocos Island. Grey solid lines indicate depth contours at 1000 m intervals. (f) Level 3 grid over Cocos Island. Grey solid lines indicate depth contours at 500 m intervals and grey dotted lines indicate depth contours at 1 m intervals.

plane. The strike in both models is 324° and the dip in both models is 7.5°, which is adopted from Paper 1 and is based on regional seismic reflection imaging [*Singh et al.*, 2011]. The fine-grid fault model (Figure 3a) has 7×15 subfaults along dip and strike directions, respectively, with subfault dimensions of 15×15 km^2. The total fault area for this model is 225×105 km^2. The hypocenter is located at the fifth row along dip and fifth column along strike. The coarse-grid fault model (Figure 3b) has four subfaults along dip and eight subfaults
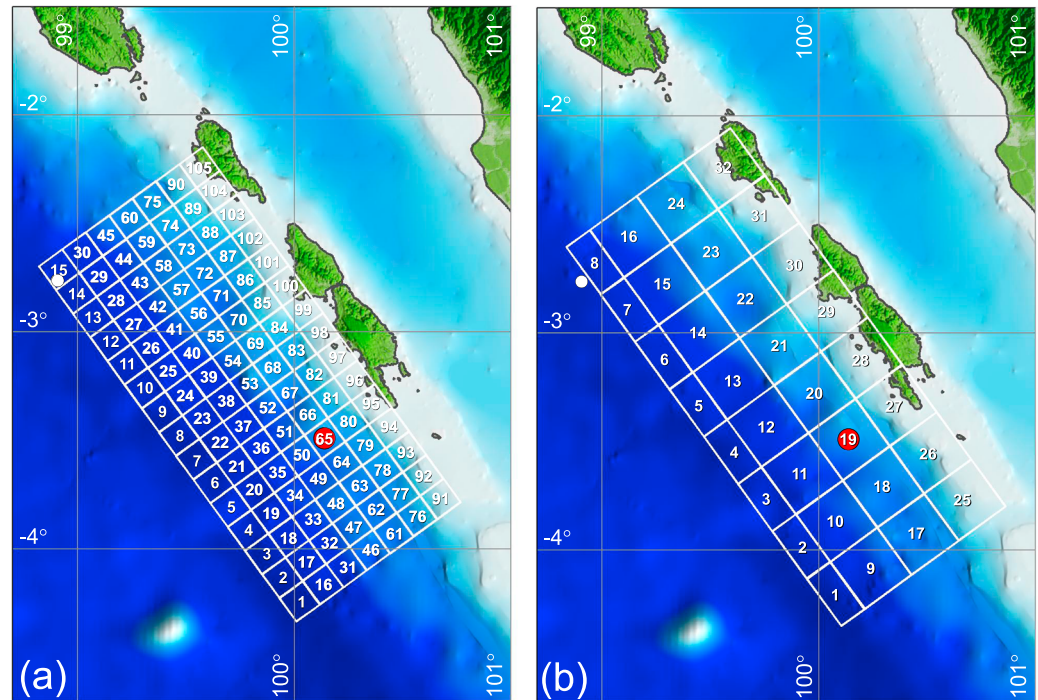
Figure 3. Source model discritizations for generation of tsunami Green's functions at the four water level stations and joint inversion with seismic and geodetic data. (a) A 105 subfault parameterization (15 columns and 7 rows) with subfault areas of 15×15 km^2. We call this the "fine-" grid model. (b) A 32 subfault parameterization with subfault areas of 30×0 km^2 for the three downdip rows and 15×30 km^2 area for the shallowest updip row. We call this the "coarse-" grid model. The red dots indicate the subfaults containing the event hypocenter.

along strike. The subfault dimensions for the first row are 15 km along dip and 30 km along strike, while the dimensions are 30×30 km^2 for the deeper rows. The total fault area is thus 240×105 km^2. The hypocenter locates at the third row along dip and third column along strike. Variable rake of each subfault subevent can be allowed by solving for weights of Green's functions computed for two distinct rakes.

The shock-capturing dispersive wave code NEOWAVE of *Yamazaki et al.* [2009, 2011a] is used to calculate the tsunami from its generation by unit slip at each subfault through propagation to each water level station. The computation involved a system of two-way nested grids with resolution varying from 1 arc min (~1800 m) across the Eastern Indian Ocean to 0.3 arc sec (~9 m) at Padang Harbor and 1.5 arc sec (~45 m) at Cocos Island as illustrated in Figure 2. The digital elevation model comprises the 30 arc sec (~900 m) General Bathymetric Chart of the Oceans from The British Oceanographic Center, the 2 arc sec (~90 m) Digital Bathymetric Model of Badan Nasional Penanggulangan Bencana, Indonesia, 1 arc sec (~30 m) Shuttle Radar Topography Mission from German Aerospace Center, 0.15 arc sec (~5 m) lidar data at Padang from Badan Informasi Geospasial, and a 9 arc sec (~250 m) gridded data set in the Cocos Island region from Geoscience Australia. In addition, we carefully redigitized the coastal boundaries and nearshore bathymetry at Padang Harbor and Cocos Island based on orthoimages and nautical charts. We assume fixed-wall boundary conditions on the coastlines and do not model local inundation effects in the tsunami Green's functions used in the inversions. The waves reaching Padang pass through the deep channels and should have little effect from overland flow at Pagai shores. In addition, inundation distances on Pagai are short relative to the wavelengths of the tsunami, so effects on the signals at the tide gauge will also be small.

The planar fault model of *Okada* [1992] is used to compute Green's functions for subfault subevents. Superposition of spatially and temporally distributed subfault contributions defines the kinematic seafloor deformation. We use a 4 s rise time for the subfault Green's functions for the seafloor displacement and velocity for the initial tsunami modeling. The staggered finite difference code builds on the nonlinear shallow-water equations with a vertical velocity term to account for weakly dispersive waves and a momentum conservation scheme to describe bore formation. The vertical velocity term also accounts for the time sequence of seafloor uplift and
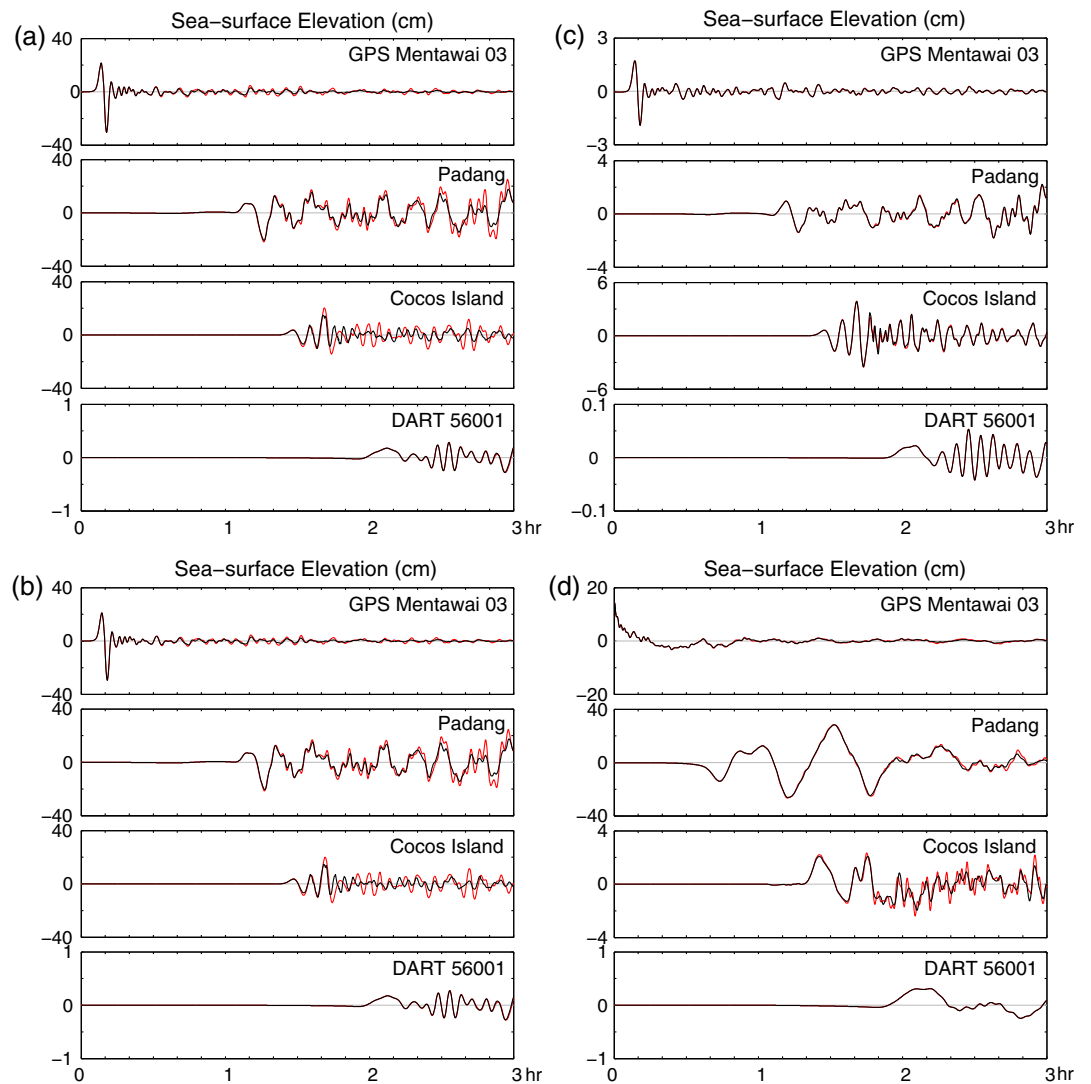
Figure 4. Comparison of linearly combined Green's functions for 1 m slip (red dashed lines) with full-scale NEOWAVE output (black lines) for (a) 10 m slip at subfault 12 (coarse grid) with 4 s rise time and 45° rake, (b) 10 m slip at subfault 12 with 40 s rise time and 45° rake, (c) 1 m slip at subfault 12 with 4 s rise time and 90° rake, and (d) 1 m slip at all subfault with 4 s rise time and 45° rake.

subsidence, while the method of *Tanioka and Satake* [1996] approximates the vertical motion resulting from the seafloor horizontal displacement on a slope. Although the hydrodynamic code and tsunami generation mechanism are nonlinear, the seafloor displacement is negligible compared to the water depth and the resulting tsunami amplitude is small even at the Cocos Island lagoon. The computed Green's functions possess the overall linearity required by the inversion routine, but we explore the details for each observing site.

3.3. Tsunami Wave Linearity Tests

Here we focus on the scaling and dispersion properties of the Green's functions relative to nonlinear model results at the four water level stations through a series of tests. The linear assumptions implicit in kinematic rupture process inversions include scaling of the Green's functions with slip or moment for each subfault, linear combination of motions for slip at different times, representation of variable rake by two reference slip vectors on the same subfault, and superposition of motions for slips on different subfaults. We examine these properties using the coarse-grid Green's functions, which have larger amplitudes compared to those from the fine grid and are more critical for the linearity test. Figure 4a compares the linearly scaled Green's function and the nonlinear NEOWAVE results for 10 m slip at subfault 12 with 4 s rise time and 45° rake. Both sets of

results are nearly identical at the GPS and DART buoys due to linearity of tsunami waves in the deep ocean. The discrepancy in the short-period codas at the Padang and Cocos Island tide gauges likely arises from nonlinear effects in shallow water. Figure 4b shows results using the same slip and rake at subfault 12, but with a 40 s rise time. The Green's function, which corresponds to 1 m slip and 4 s rise time, is shifted and summed at 4 s intervals to mimic the 10 m slip over 40 s. The results are almost identical to those linearly scaled from the Green's function as shown in Figure 4a. The comparison of the nonlinear results between the two cases confirms that the waveforms are relatively independent of the rise time up to 40 s. The minor phase shift introduced by the 40 s rise time has negligible effects on the computed tsunami with periods of over 10 min.

The finite-faulting inversion routine resolves variable rake at each subfault by using a pair of Green's functions computed for unit slip with distinct rakes; for the tests here we use 45° and 135°. Figure 4c shows that the linearly combined Green's functions from the two orthogonal components at subfault 12 are nearly identical to the NEOWAVE results computed for 90° rake with the same resultant slip and rise time. The agreement at the Padang and Cocos Island tide gauges are much improved compared to the earlier tests because of negligible nonlinear effects associated with the much smaller wave amplitude. The final test involves uniform 1 m slip of the entire rupture grid for 45° rake and 4 s rise time. The linear and nonlinear results in Figure 4d show very good agreement. The large fault dimensions compared to the water depth result in minimal oscillations at the source after the initial pulse in accordance to long-wave theory. The linearly combined Green's functions are able to reproduce the increased wave periods due to the large fault area and subsequent arrival or development of shorter-period waves at the far-field water level stations.

Linearity holds up well for the two deep ocean tsunami records (GPS buoy and DART 56001) and the results are consistent with expectations for deep ocean records. For the Padang tide gauge record, the nonlinear effect is apparent for the coda waves, consistent with their generation by reflection near the coasts, where nonlinear effects are expected to be significant. For the initial peak of the Padang record, which is used in the finite-fault inversion, linearity is valid. The Cocos Island record shows a more complex pattern than other records. When the wave amplitude at Cocos Island approaches 20 cm, nonlinear effects show up in the initial peak, while when the wave amplitude is ~5 cm, linearity holds up well. Given that the water depth near Cocos Island ranges from 2 to 5 m, 20 cm approaches 10% of water depth, which is a limiting criterion for linearity. For the Mentawai earthquake, given that the maximum slip is > 10 m, and peak wave amplitude is ~20 cm, significant nonlinear effect is expected for the Cocos Island recording. With the maximum wave amplitude at Padang tide gauge being ~40 cm, linearity is valid for the Mentawai event, but may break down for larger events.

NEOWAVE generates the Green's functions from kinematic seafloor deformation in contrast to the common approach that utilizes the coseismic seafloor displacement as the initial conditions at the sea surface. Because of dispersion, the excitation from the seafloor attenuates over the water column and the sea surface has a smaller vertical displacement [*Lay et al.*, 2013a, 2013b, Paper 1]. Since the dispersion of the seafloor excitation becomes more significant as the water depth to fault-scale ratio increases [*Kaijura*, 1963], we utilize the fine grid to examine its impact on the resulting Green's function. Figure 5 compares the Green's functions generated by kinematic seafloor deformation and static initial conditions for 1 m slip and 45° rake at subfaults 8, 11, 13, and 15 along the first row of the fine grid. The rise time of 4 s associated with the seafloor deformation has negligible effects on the long-period tsunami waves to enable direct comparison of the two data sets. In Figure 5a, the Green's functions at the GPS buoy illustrate their evolution with travel distance. The GPS buoy is located at subfault 15. The smaller initial pulse from seafloor excitation is due entirely to dispersion during the generation process. In contrast, the large short-period initial pulse from the static initial condition is more dispersive during propagation. By the time when the initial pulse from subfault 8 reaches the GPS buoy, it has the same amplitude as the one generated by seafloor excitation. The larger initial trough and coda are due to more energetic oscillations at the source resulting from free fall of the larger, initial sea surface wave. These source effects are evident at far-field locations such as Padang and Cocos Island as shown in Figures 5b and 5c. The Green's functions generated by the two approaches are gradually converging and become very similar at the DART buoy 1600 km from the source (Figure 5d).

The sensitivity tests have illustrated the linearity and scalability of the Green's functions for adaptation into the finite-fault model. The present nonhydrostatic approach with seafloor excitation provides a more realistic
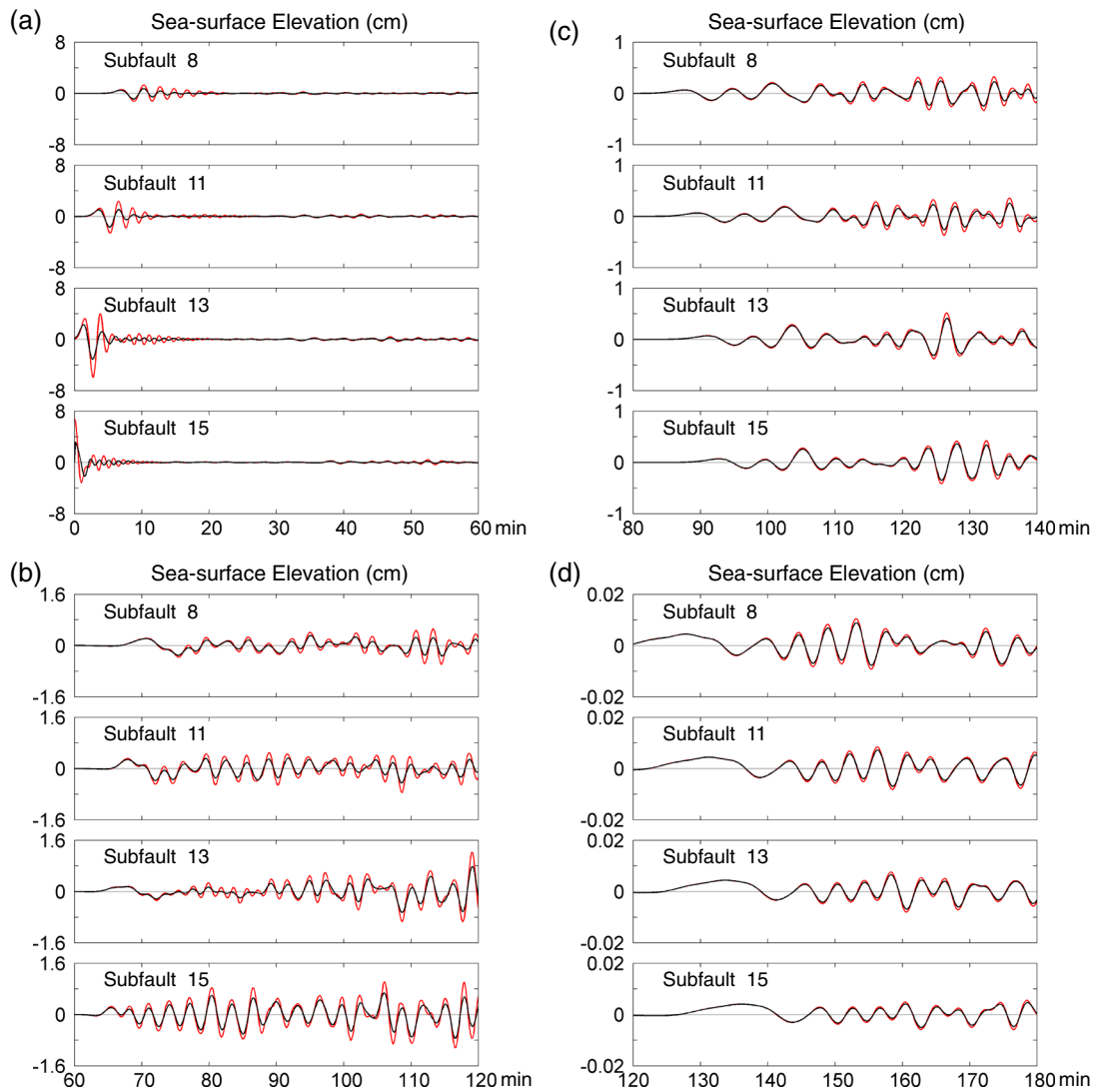
Figure 5. Comparison of Green's functions generated by kinematic seafloor deformation with a 4 s rise time (black lines) and static sea surface deformation as initial conditions (red lines). (a) GITEWS GPS. (b) Padang tide gauge. (c) Cocos Island tide gauge. (d) DART 56001. The subfault number refers to the fine grid in Figure 3a, and the Green's functions correspond to 1 m slip with 45° rake. The final kinematic seafloor deformation and the static sea surface deformation are identical. The Green's functions generated by kinematic seafloor deformation have smaller initial amplitudes in the near field due to horizontal motion of the displaced water and subsequent attenuation of the vertical displacement to the ocean surface. Dispersion during propagation gives rise to similar initial wave amplitudes of the two sets of Green's functions in the far field. The free fall of the larger sea surface wave from the static initial conditions contributes to more energetic oscillations at the source and larger amplitudes of the codas.

description of the Green's functions in the near field, which play a significant role in the inversion of the Mentawai tsunami. We therefore move on to describing the inversion technique in more detail.

4. Inversion Method

For finite-fault inversions, we utilize Green's functions computed for a reference slip (or seismic moment) over specified subfault areas with given strike, dip, rake, and depth. The finite-fault inversion involves solving for space-time varying weights of the Green's functions to match the recorded data. Kinematic models, for which the rupture expansion is specified and subfaults have prescribed source time function representations, can be formulated as a linear least squares inversion for the model weights (seismic moment of each subfault subevent for a given slip geometry) [e.g., *Hartzell and Heaton*, 1983]. For joint inversions of time-varying seismic, hr-GPS and tsunami signals, the linear least squares approach further requires relative data-type

weighting and a model parameterization (discretization and regularization) that accommodates the varying intrinsic characteristics of the different data types, as discussed later.

4.1. Subfault Parameters

For each coarse-grid subfault, the source time function is parameterized by 20 triangles with rise times of 2 s and shifted by 2 s sequentially, allowing 42 s long subfault source time functions. We adopt shorter source time function durations for each fine-grid subfault, because the rupture propagation time over the smaller subfaults is shorter. The source time function is parameterized by five triangles, with rise times of 2 s and shifted by 2 s sequentially, allowing 12 s long subfault source time functions. Green's functions for two slip vectors with rakes of 85° and 115° are used for all data types in each case, with the positivity constraint in the least squares inversion limiting the subfault slip vectors to within this range. Usually, we allow a rake angle variation of 90° for variable rake rupture model inversions; however, we found that tsunami waves are less sensitive to the particular rake angle at each subfault than to the ocean floor uplift location. We therefore constrained the range of rake angle variation to 30° for the joint inversions with tsunami data to maintain solution stability relative to the point source faulting parameters. Our Paper 1 modeling found only minor rake variations between subfaults, so this is not an overly restrictive constraint. The number of unknowns in the fine-grid model is 1050, comparable to the 1280 unknowns of the coarse-grid model.

Tsunamis are predominantly low frequency waves that are not sensitive to small-scale details of the rupture pattern. For general tsunami inversions, the coarse-grid parameterization with subfault scale of 30 km is adequate to represent the tsunami excitation, but use of relatively large subfaults imposes intrinsic constraints on the finite-fault model that must be considered for each data type used. For example, the near-field tsunami waveform from the GPS buoy shows two peaks that might indicate fine variation in the slip distribution that we may need the fine grid to resolve. Kinematic rupture models involve a subfault rupture initiation time defined by a specified rupture velocity, typically initially activating subfaults when the rupture expansion front reaches the subfault midpoints defined by the model grid. With large grid spacing, and low rupture velocity, long subfault source durations are required to provide sufficient model flexibility to match the teleseismic signals and the time-varying motions in the hr-GPS signals. To partially reduce the artificial spatial segmentation of the rupture for the coarse grid, we allowed subfaults to initially be activated when the rupture front reaches the grid edges to reduce the initial time discrepancy between fine- and coarse-grid settings caused by different grid scales.

4.2. Tsunami Wave Time Correction

It is desirable to use absolute time in inversions of deep ocean tsunami records to fully exploit their ability to constrain the rupture location, and this requires accuracy of the traveltimes in the Green's functions [*Yue et al.*, 2014b]. Precise bathymetric models are required, particularly for waves traversing shallow water. Even with accurate bathymetry models and dispersive tsunami modeling techniques the results might show up to ~1% overestimation of wave velocity leading to accumulating traveltime error with distance. This might be caused by shoaling and bore propagation errors, the absence of coupling between the tsunami gravity wave and solid medium elasticity, and not accounting for water density variation with depth [e.g., *Bai and Cheung*, 2013a, 2013b; *Tsai et al.*, 2013; *Allgeyer and Cummins*, 2014; *Watada et al.*, 2014]. Frequency dependent traveltime corrections can be applied to the Green's functions from tsunami codes like NEOWAVE and COMCOT to account for elasticity and water density effects for distant tsunami stations in some cases, enabling use of absolute times [e.g., *Yue et al.*, 2014b].

For the Mentawai event, arrival time discrepancies are significant for the tide gauge observations (~2 min at Padang and ~4 min at Cocos Island), and application of dispersive velocity corrections does not account for the arrival time anomalies. Although we use detailed bathymetry models near Padang and Cocos Island (Figure 2) for precise waveform modeling, very detailed bathymetry models are not available for the entire path, and the specific cause of the traveltime errors is uncertain. We believe that shoaling and bore propagation errors are major factors causing the respective time shifts observed at the Padang and Cocos Island tide gauges. This limits the use of absolute times in the inversions, and for the Padang and Cocos Island tide gauge observations, relative arrival time is used instead of absolute arrival time. In our algorithm, we grid search for the optimum time shifts of the predicted signals at Padang and Cocos Island stations to fit the data in a relative time frame. Time shifts of 140 and 250 s, respectively, are found in the search technique, providing minimum tsunami misfits when other parameters are fixed.

When computing tsunami Green's functions, the ocean floor displacement is computed by a half-space model [*Okada*, 1992], which drives the tsunami excitation. Shallow layered structure with low-velocity sediments can influence the ocean floor deformation and tsunami wave height. We applied a linear-scaling correction between the half-space model and a layered model [*Wang*, 1999; *Wang et al.*, 2003], to scale the half-space tsunami Green's functions for consistency with the layered structure used in modeling the teleseismic body waves and hr-GPS signals (Paper 1). The amplitude of this correction is 5–15%, and it has negligible frequency dependence in the tsunami frequency band. One could compute the tsunami excitation with the layered structure directly to avoid this correction, but for this case our correction accounts for most of the effect.

4.3. Tsunami Time Window

Selection of the tsunami signal time window for inversion is also a distinct challenge relative to the other data types. For the hr-GPS data set, the waveforms stabilize after the surface waves pass by, and the choice of time window length does not influence the inversion results significantly as long as all dynamic waves are included. For teleseismic body waves, a time window that includes the entire rupture duration and arrivals of surface reflected phases but excludes secondary arrivals not included in the Green's functions like *PP* or *SS* is adequate for the inversion. However, the direct source-generated signal is not always easy to delimit in tsunami records, especially for the tide gauge recordings. For a simple thrust fault dislocation source, the initial tsunami wave mirrors the water height uplifted by coseismic ground deformation and generally involves a single dominant peak and its associated side lobes, although this does depend on the station azimuth. As demonstrated in many studies, we find that including the first peak and its following trough is usually sufficient to capture the main rupture process, with later arrivals tending to be dominated by propagation complexities and shelf resonance. The linearity tests in section 3 have also verified the Green's functions in reproducing the initial peak and trough at the two tide gauges from NEOWAVE. For the 2010 Maule, Chile, and 2014 Iquique, Chile, earthquakes, for which we inverted only far-field deep ocean tsunami records jointly with seismic and geodetic data, this strategy worked well [*Yue et al.*, 2014b; *Lay et al.*, 2014].

The dominant long-period pulse at DART station 56001 is readily windowed. Windowing the other Mentawai tsunami recordings is more complex. The nearby GPS buoy recording has a double peak, indicating two isolated locations of concentrated seafloor uplift, and our windowing is such that it spans the full rupture process and propagation times from the farthest subfaults. The tide gauge recordings at Padang and Cocos Island are complex. Paper 1 demonstrated that the modeled tsunami is valid for predicting the first several cycles of the arrivals at Padang and Cocos Island but failed to predict the waveforms later than 1000 s after the initial peak. Thus, we adopt a time window including the first peak and trough at Padang and the first three peaks of the Cocos Island record. We find that using longer time windows does not impact the slip pattern significantly because the coda waves are never well fit, but it is sensible to constrain the inversion to the interval for which the Green's functions are most valid. The inversion time windows could be extended given more precise Green's functions; however, the initial waveform cycles provide information directly from the source rather than involving reflected or diffracted waves as is desirable for the joint inversions.

4.4. Teleseismic Data Set

We use the same teleseismic body wave data set as in Paper 1, which is comprised of 53 *P* wave and 24 *SH* wave ground displacement recordings from stations of the Federation of Digital Seismic Networks (FDSNs), accessed through the Incorporated Research Institutions for Seismology (IRIS) data management center. The data are selected from hundreds of available FDSN seismograms to ensure good azimuthal coverage and high signal-to-noise ratios, for epicentral distances from 40° to 90°. Instrument responses are deconvolved to provide ground displacement with a band-pass filter having corner frequencies of 0.005 and 0.9 Hz. One hundred twenty second long time windows are used with time sampling of 0.5 s, starting 10 s prior to initial *P* or *SH* arrivals. The *P* wave signals provide information about seismic radiation for periods as short as several seconds but are very depleted in shorter-period energy due to the source process. The teleseismic Green's functions are generated with a reflectivity method that accounts for interaction in 1-D layered structure on both the source and receiver sides [*Kikuchi et al.*, 1993]. The local 1-D layered model is used for the source side, and a typical continental model is used for the receiver side. The same band-pass filter used for the data is applied to the Green's functions.
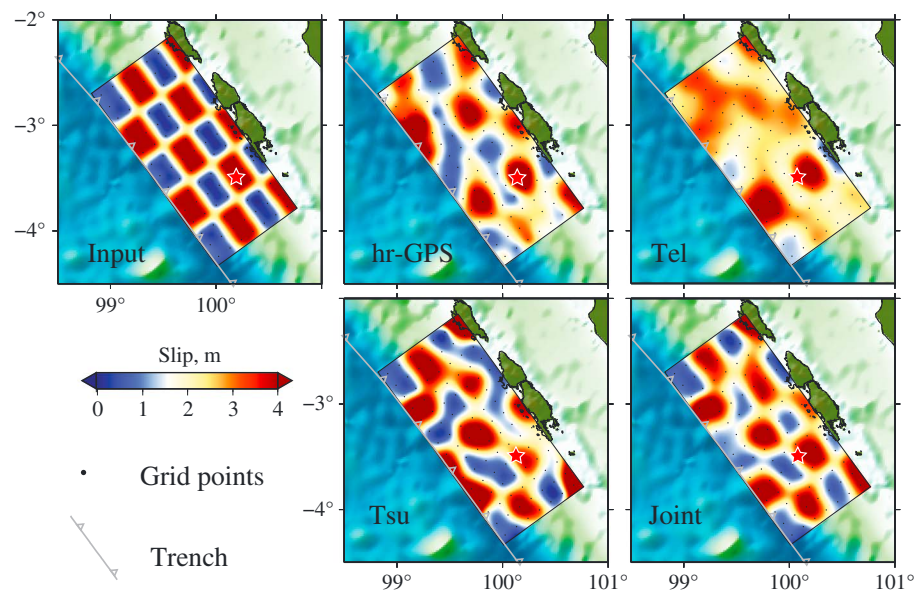
Figure 6. Checkerboard tests of linear inversions for each data set separately and jointly. The input model is shown in the top left panel. Separate and joint inversion results of hr-GPS, teleseismic (Tel), and tsunami (Tsu) data sets are shown in the four right panels. Color scale for the slip pattern is plotted at the lower left. Grid points are plotted with black-filled circles in each panel. The fine grid is used.

4.5. The hr-GPS Data Set

We use the three-component ground motion solutions for 12 high-rate SuGAr GPS stations presented by *Hill et al.* [2012]. The high-rate (1 s sampling) kinematic GPS solutions are generated using Precise Point Positioning mode in the GIPSY-OASIS II V6.0 software [*Zumberge et al.*, 1997]. Details of the processing and comparisons with daily (averaged over 24 h) solutions are provided in *Hill et al.* [2012]. The time-varying signals in these hr-GPS signals include body and surface wave arrivals emanating from the entire slip zone that help to constrain the space-time distribution of slip.

To model the time-dependent near-field ground displacements recorded by hr-GPS, Green's functions for the full dynamic and static elastic deformation field must be used. We use the Green's functions database computed in Paper 1 using a frequency-wave number (F-K) integration method that includes all near-field terms (Computer Programs in Seismology, Robert Herrmann). These are for the same local 1-D layered model as used for the teleseismic calculations. The database was generated for epicentral distances of 0 to 500 km and source depths of 0 to 50 km with 1 km increments for distance and depth. We use the nearest Green's functions for each source grid node for each station, incurring minor errors (<0.5 km) in propagation distance. Both Green's functions and data are low-pass filtered at a corner frequency of 0.1 Hz, to eliminate any short-period multipathing artifacts in the hr-GPS data processing, as well as any short-period propagation effects not accounted for by the 1-D velocity structure. Each trace has a 200 s long time window, starting at the origin time of the hypocenter and 1 s time sampling.

4.6. Checkerboard Test

Checkerboard tests for separate and joint inversions of teleseismic, hr-GPS, and tsunami observations provide a way to establish the sensitivity of each data set to the slip distribution [e.g., *Lorito et al.*, 2011; *Yue et al.*, 2014b]. The sensitivity to slip pattern depends strongly on the specific distribution of observations, the complexity of the Green's functions and their accuracy, the wave velocities and frequencies of the dominant signals, and the choice of regularization used for the inversion.

Checkerboard tests for inversions of the Mentawai data sets are shown in Figure 6. We introduced 10% uniformly distributed random noise to the synthetics, and 10% overestimated rupture velocity was used in the inversions. In generating the synthetics from the respective Green's functions, we used 4 s duration source time functions for each subfault, while in the inversions we allow up to 10 s long subfault total source

durations, which provides some freedom for the inversions to adjust the rupture time for the error in assumed rupture velocity. The smoothing and relative weighting are the same as for the joint inversion in each case. The hr-GPS data have high sensitivity to the downdip slip distribution close to the islands, but limited resolution of slip near the trench. The teleseismic data set has relatively good spatial resolution near the hypocenter, because for the rupture initiation there are not many parameters to produce space-time trade-off. For later rupture, the resolution is limited. The tsunami data set provides quite good resolution of near-trench slip, as expected. For the Mentawai event, the fault plane is extended only to under the seaward coast of the Pagai Islands because any deeper slip would produce strong hr-GPS signals and early tsunami arrivals at Padang, neither of which are observed. Thus, in this case, the tsunami data do have some resolution of the downdip rupture pattern. The tsunami data set appears to provide some resolution of the slip pattern over the entire fault plane, but it is not sensitive to the fine details of the slip pattern because of its low-frequency content. The joint inversion can combine the advantages of all data sets, yielding a rupture pattern and slip magnitude closer to the input model compared with any separate inversion results.

4.7. Relative Data Set Weighting

The data weighting used in joint inversions has a strong influence on the resulting models. Each data set has different sensitivity to aspects of the rupture, thus relative weighting between data sets influences which features are emphasized. Relative weighting is not only dependent on the intrinsic errors in each observation but also relies on the accuracy of the Green's functions, which is hard to determine without knowing the exact Green's functions. The general strategy we use to specify relative data set weighting is to fix one data set to be normally weighted and then adjust the relative weighting of other data sets. A preferred relative weighting is found for the minimum point of the "U-" shaped weighting versus residual curve, which indicates that useful information in either data set is equally weighted. Following this strategy, a 1:1 weighting between hr-GPS and teleseismic data sets was selected in Paper 1. A similar strategy is used when tsunami data are incorporated in the joint inversion, but all data sets have to be balanced. Because the tsunami waveforms are rather simple pulses, the data intrinsically prefer smooth slip patterns. If tsunami data are equally weighted, the waveform fitting of other, shorter-period data sets is strongly impacted. Exploring the waveform fitting and slip pattern leads us to select a relative weighting of 0.5 for the tsunami data set. Thus, our preferred relative weighting for hr-GPS, teleseismic and tsunami data sets is 1:1:0.5. This relative weighting is subjective, as usual, and is not meant to be a general result. The degree to which complementary data sets stabilize the solution for aspects of the model poorly resolved by other data sets is not fully captured by separate measures of data fitting or variance reduction, so we advocate empirical exploration of weighting choices.

Including tsunami waves introduces the additional complexity of relative weighting between stations, given the different sensitivity of each type of tsunami recording in our case. Limitations of the propagation model means that tide gauge observations are harder to model, and this is compounded by the limitations of linearity assumptions. In our inversions, the relative weighting between the GPS buoy, DART 56001, Padang, and Cocos Island is selected to be 1:10:0.2:0.2, which is arrived at by performing tens of inversions with different weighting parameters. The preferred weighting values are based on striving to balance individual data contributions to resolving parts of the model that they are most sensitive to without allowing their insensitivity to other parts of the model to overwhelm complementary sensitivity from other data sets. This is very difficult to treat theoretically or formally, so our approach was empirical. This is also true of relative weighting of different data sets in the joint inversions.

4.8. Rupture Velocity

When the data sets used in joint inversions all provide some resolution of temporal and spatial rupture characteristics, a rupture velocity versus residual curve can be used to establish the optimal rupture velocity from the trade-off curve [e.g., *Yue et al.*, 2013]. A similar strategy is adopted for inversions with the fine and coarse grids. A preferred rupture velocity of 2.0 km/s is found for both fine and coarse grids, from the turning points of the trade-off curves.

4.9. Model Regularization

For kinematic rupture models inverted with the multitime window method, the fault model is generally overparameterized, which makes the problem underdetermined. Various regularization techniques are adopted in finite-source inversions to stabilize the inversion results. Relative to the fine-grid inversion, the
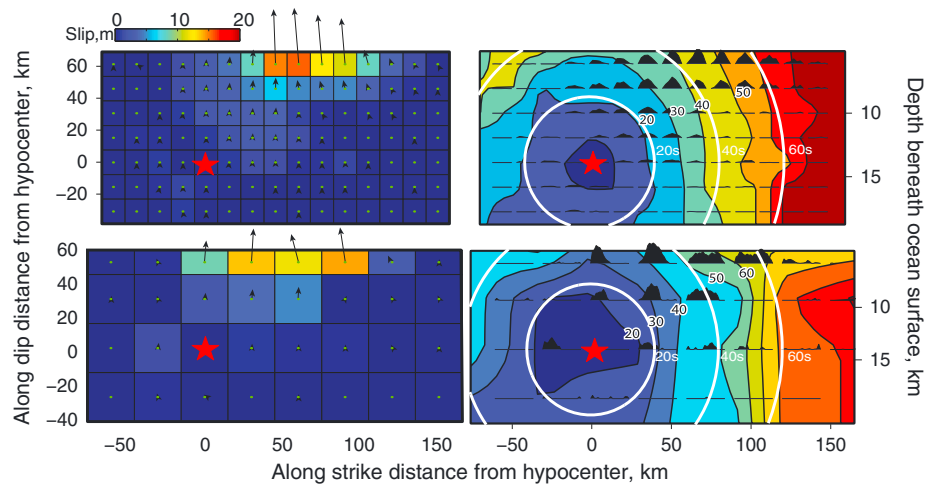
Figure 7. Slip pattern and subfault source time functions for inversions with the fine and coarse grids are shown on top and bottom rows, respectively. Slip patterns are shown on the left column and subfault source time functions maps are shown on the right column. The hypocenter is marked with a red-filled star in each panel. Grid points are plotted with green dots, with the subfault areas indicated on the left. Total slip in each subfault is indicated with a blue/red color scale, and slip magnitude and direction are indicated with black arrows. Subfault source time functions and rupture timing are shown on the right. Rupture fronts defined by the input rupture velocity (2.0 km/s for both fine and coarse grids) are plotted with white concentric circles with 10 s isochrones. Source time functions of each subfault are plotted with black-filled polygons with maximum durations of 12 s and 42 s for the fine and coarse grids, respectively. The region of slip distribution for increasing centroid times labeled in black is contoured with blue to red color scale (different from the slip scale).

coarse grid has intrinsically more regularization, accounting for the heterogeneous rupture process by the long time-varying subfault source time functions. Thus, additional spatial or temporal smoothing of the solution may not be necessary. In our tests of the joint inversion for the coarse grid, the various data sets appear to provide enough resolution that no further regularization is needed to produce stable results that fit the data well. For the fine-grid case, the grid spacing of 15 km is close to the limit of the spatial resolution of the data sets given the time sampling and apparent velocities of the dynamic terms, so some regularization is necessary. We adopted a minor Laplacian smoothing factor of 0.1 as it produces a slip pattern and peak slip consistent with the unsmoothed coarse-grid inversion result. There remain trade-offs between smoothing, grid size, and slip location for variable model discretizations, and the data do not suffice to give a unique preference. We explored a wide range of smoothing factors, developing an empirical sense for the impact on fitting of different data sets and overall model complexity.

5. Results and Discussion

5.1. Preferred Rupture Models

Our preferred inversion results for both the fine- and coarse-grid models are shown in Figure 7. The overall slip patterns for both results involve unilateral rupture propagation updip and along strike in the northwestward direction, with distributed shallow slip along the trench. For the fine-grid, peak slip of ~15 m is located ~60 km along strike from the hypocenter in the near-trench row. Distributed slip is resolved between the hypocenter and updip slip patches with average slip of ~5 m. For the coarse grid, the near-trench large-slip area extends ~100 km along the strike direction, with similar average slip of ~15 m. The slip pattern for the coarse grid is quite regular despite the lack of smoothing. Averaged slip of ~5 m is again found in the region between the hypocenter and updip slip concentrations. The cumulative seismic moment is 8.76×10^{20} N m (M_w 7.90) and 8.08×10^{20} N m (M_w 7.87) for the fine- and coarse-grid models, respectively. So the slip distributions and seismic moments are generally consistent for the two models. The temporal rupture propagation pattern is slightly different, which is expected given the larger grid size and longer subfault source time functions for the coarse model. Slight differences in the centroid time contours are caused by the grid spacing differences. However, the contouring for varying centroid time shows good consistency between the models, with both the main energy release between 20 s to 60 s. The resulting kinematic fault model parameters are provided in the supplementary materials for both fine- and coarse-grid settings.
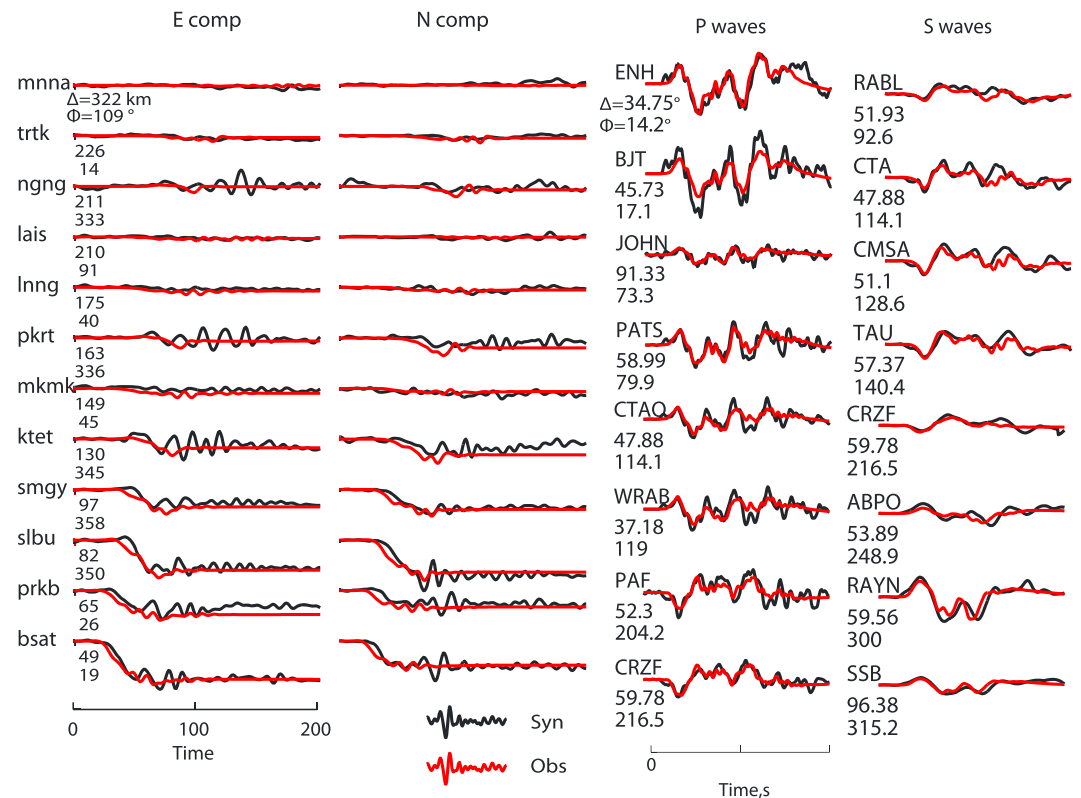
Figure 8. Observed (red) and modeled (black) ground displacement signals for hr-GPS and selected teleseismic *P* waves and *S* waves for the preferred fine-grid joint inversion. Only horizontal components of the hr-GPS records are shown, ordered by epicentral distance. Teleseismic records are ordered by azimuth.

5.2. Waveform Fitting and Data Sensitivity

Comparisons of observed and computed waveforms for the fine grid inversion are plotted in Figures 8 and 9. Both the early dynamic and static portions of the hr-GPS observations are well modeled (Figure 8). The hr-GPS records show some significant arrivals after 80 s that are not well matched, as was the case in Paper 1. We believe these are not features caused by the main rupture. These arrivals do not have clear static offsets and lack consistent moveout between stations, so they may be caused by secondary scattered energy or very local triggered events near the stations off the main fault plane. The fits to the teleseismic P and SH waves are comparable to the joint inversions of hr-GPS and body waves performed in Paper 1. It is likely that the errors incurred by using 1-D velocity model Green functions delimit the body waveform fitting.

Figure 9 shows the waveform fits to the tsunami observations for the fine grid joint inversion, along with the waveform contributions from separate slip patches. The overall fits are quite good, compatible with the fits to the other data sets. Residuals of waveform power for the hr-GPS/teleseismic/tsunami misfits are 9%/37%/22% for the fine grid, which are similar to residuals (8%/27%/20%) for the coarse-grid model (while the coarse-grid model has more parameters, it is also less kinematically constrained overall due to the long subfault durations used).

The slip distribution was subdivided into three subregions, covering the large-slip concentrations near the trench and the region of lower distributed slip between the hypocenter and the trench. The tsunami wave contributions produced by each subregion are plotted below the complete waveforms in Figure 9. The waveform contributions to the two pulses in the GPS buoy observations are quite distinct, with the waveform of the third patch, closest to the buoy, accounting for the first peak and the waveform of the second patch accounting for the second peak. The deeper distributed slip patch also contributes to the second peak and the trough after the first two peaks. In previous studies, two separate slip patches near the trench have been inferred based on the two pulses recorded at the GPS buoy [Paper 1; *Satake et al.*, 2013b]. Here we find that the two peaks can be well fit with a relatively distributed slip patch similar to that used in *Hill et al.* [2012].
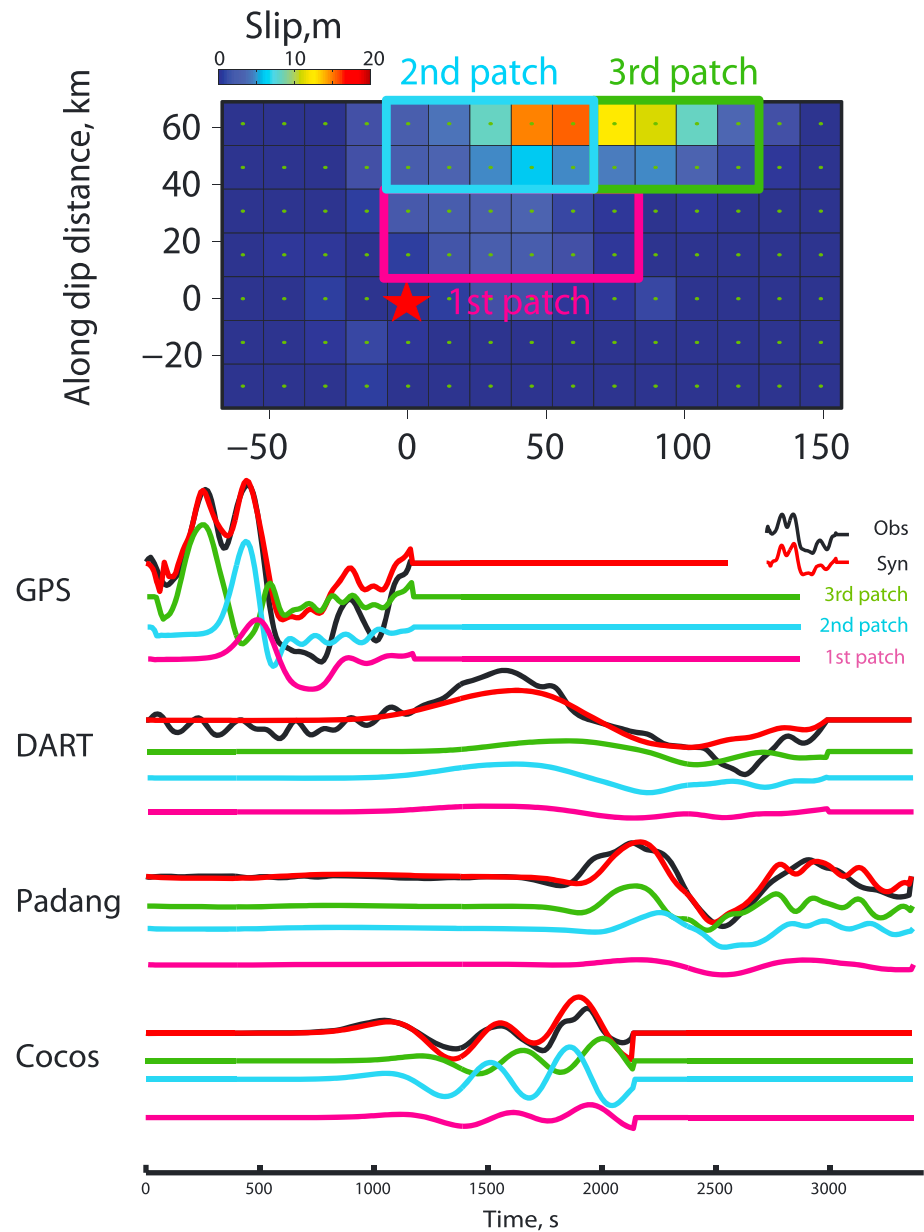
Figure 9. Waveform fits for tsunami recordings showing contribution from separate slip regions for the fine grid. (top) Three slip patches are bounded by frames and marked in different colors. (bottom) Observed and synthetic tsunami waveforms are plotted in red and black, respectively. Waveform contributions from the three patches are plotted in their associated color below the waveforms of each station.

The space-time evolution of slip over a discretized model grid with variable slip and subfault source time function is nonunique and limits our resolution of slip heterogeneity. For DART 56001 the first and second patches contribute to the main pulse, as these are closer to the station. For Padang, all three patches contribute to the first peak and trough with slightly different arrival times. The waveform fits to the Cocos Island recording involve interfering contributions, with the initial peak mainly contributed by the second patch, since it locates closest to this station. The waves from the third patch arrive later than the second patch and the shifted arrival time tends to destructively interfere. Similar spatial contributions are found for the coarse-grid solution.

The primary resolution of the large-slip concentration near the trench is from the GPS buoy, for which the small epicentral distance allows recording of high-frequency tsunami waves intrinsic to the source. The Green's functions computed from the nonhydrostatic code capture dispersion and attenuation of the vertical
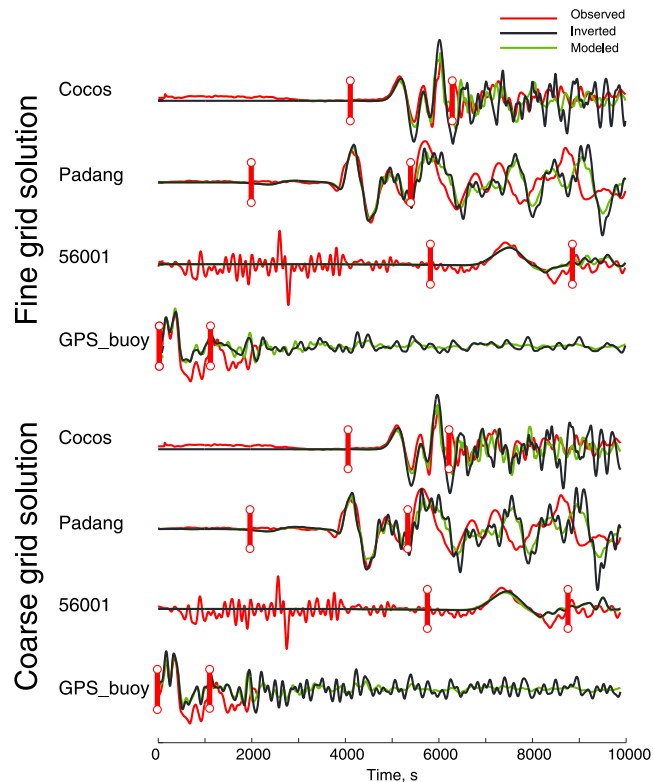
Figure 10. Comparison of observed (red) and predicted tsunami waveforms from linear joint inversion (black) and nonlinear forward modeling (green) using fine and coarse grids. Results for the referred rupture models for the fine and coarse grids are shown. Time windows used in the joint inversion are bounded by vertical bars in the top panel. For each trace, waveforms are normalized by the peak amplitude of the observations.

water displacement from the seafloor to the surface and accurately resolve the slip distribution from the near-field tsunami record. Assumption of identical sea surface and seafloor coseismic vertical displacement is implicit in the Green's functions generated by hydrostatic codes. Their application in an inversion routine will likely lead to lower predictions of the near-trench slip, as in some prior studies of this event.

5.3. Testing of Linear Validity for the Full Models

As a final test of the validity of linearity assumptions, we computed fully nonlinear tsunami waveforms for the final preferred models at the four water level stations. Cumulative slip for each subfault is taken from the inversion results, along with the total subfault source time function durations, for the Okada model calculations. The computed seafloor displacement is not sensitive to the detailed subfault source time functions, which is acceptable given the low-frequency nature of the tsunami data. The full tsunami modeling for the results of inversions with fine and coarse grids are compared with the data in Figure 10, along with the predictions from the inversion.
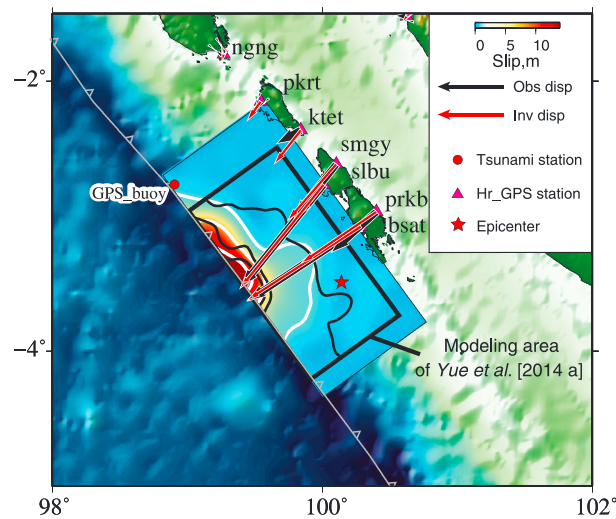
The waveforms from full modeling and inversion output at all stations are very consistent for both inversion solutions, which indicates validity of linearity, particularly for the waveform interval used in the inversions. The full waveform modeling for Cocos Island matches the inverted portion of the data very well, actually better than the inversion output. The linear assumption in our inversion appears to somewhat overestimate the large downswing, but this is reduced in the fully nonlinear calculation. The excellent fit may be somewhat fortuitous, but it indicates that the solution is not significantly biased. With the amplitude of the Cocos Island data being downweighted by 0.2 in the inversion, any nonlinearity affecting the Cocos Island waveforms does not impact the inversion significantly.

5.4. Comparison With Iterative Inversion Results

As we are using the same data but a different optimization method to that of Paper 1, it is interesting to compare the model results produced by iterative forward modeling and joint inversion. The models are compared in Figure 11, where our fine-grid solution is shown. The overall slip pattern is quite consistent between these two results, with the fault rupturing unilaterally updip to the northwest. The downdip limit of significant slip in these two results, taken here as the 8 m slip contour, matches well. Both solutions show significant slip near the trench with similar extent along strike and dip directions, with minor differences in slip distribution. However, several rupture details differ between these two models.

The iterative inversion result has some distributed slip in the southeast portion of the fault plane, which is not present in the joint inversion result. The checkerboard solutions in Figure 6 show that the hr-GPS and teleseismic data sets do not have resolution in this region, so the distributed slip there is probably caused by the smearing effect of the smoothing function used in Paper 1. The iterative modeling procedure does not

Figure 11. Comparison between the slip pattern resolved by the fine-grid joint inversion (blue-red color scale) with the slip pattern from iterative inversion and tsunami forward modeling found by *Yue et al.* [2014a]. The current inversion results are contoured at 2 m, 8 m, and 14 m in red. Color scale of the coseismic slip is shown in the legend at the top right. The model area of *Yue et al.* [2014a] is bounded with a thick rectangle frame. Slip pattern of that model is contoured at 2 m, 8 m, and 14 m in black. The hr-GPS stations are plotted in magenta-filled triangles with stations names labeled. Observed (black arrows) and modeled (red arrows) coseismic displacement vectors are plotted at each station. The epicenter is plotted with a red-filled star. The GPS buoy tsunami station is marked with a red-filled circle.

suppress this feature. In the joint inversion with tsunami signals, because the tsunami data provide improved resolution of the near-trench slip, this smoothing artifact is removed. Another difference is that the peak slip amount in the iterative approach is 23 m, which is significantly higher than for other slip models. In Paper 1 it was noted that the peak slip amount in finite-fault inversions is not very stable and that the very high peak slip may be an artifact of smoothing and dynamic constraints used in the inversion, which are selected based on the iterative tsunami modeling. For this joint inversion, the peak slip amount is reduced to ~15 m for both the fine-grid model inverted with a modest smoothing function and the coarse-grid model inverted without any smoothing function (the coarseness of the grid is itself a form of regularization). While peak slip estimates are still dependent on the model parameterization, the value found here is stabilized by the joint inversion approach, so we prefer the current results.

6. Conclusions

The source process of the 2010 Mentawai M_w 7.8 tsunami earthquake is analyzed by joint inversion of tsunami, hr-GPS, and seismic waveform data. The tsunami data include a near-field deep water recording, a far-field deep water recording, and tide gauge recordings from regional and distant locations. These diverse signals allow us to examine linearity of the tsunami behavior relative to the linear nature of the seismic and geodetic inversion. The Green's functions for shallow-water tide gauge observations do show appreciable nonlinearity in terms of slip scaling for the large-amplitude signals. Stable linearity is found for the tsunami response for linear combinations of Green's functions for different rakes, different subfault rise times, and summation over multiple subfaults. Inclusion of the tsunami signals in joint inversions—as an alternative to our earlier approach of iterative model parameter optimization by sequential joint inversion of seismic and geodetic data and forward modeling of the tsunami signals—works well, as long as suitable windowing and model discretization and parameterization are applied. The near-field deep water tsunami observation and the Green's functions generated by a nonhydrostatic code from seafloor excitation are particularly valuable for resolving spatial heterogeneity in very shallow slip extending out to the trench for this event. A shallow patch of large (~15 m) slip is found at shallow depth on the megathrust, extending 60–100 km along the strike direction similar to results from iterative modeling, but with lower slip due to direct exploitation of the tsunami signals in the inversion. The 2010 Mentawai earthquake provides clear demonstration of the potential for large slip to extend to the toe of subduction megathrusts in isolated failures, not driven from large deep slip. This indicates large strain accumulation and brittle failure of the very shallow environment, in contrast to ideas of pervasive slip-strengthening frictional behavior often assumed to preclude large earthquake occurrence.

References

Allgeyer, S., and P. Cummins (2014), Numerical tsunami simulation including elastic loading and seawater density stratification, *Geophys. Res. Lett.*, *41*, 2368–2375, doi:10.1002/2014GL059348.

An, C., I. Sepúlveda, and P. L.-F. Liu (2014), Tsunami source and its validation of the 2014 Iquique, Chile earthquake, *Geophys. Res. Lett.*, *41*, 3988–3994, doi:10.1002/2014GL060567.

Avouac, J.-P., F. Ayoub, S. Wei, J.-P. Ampuero, L. Meng, S. Leprince, R. Jolivet, Z. Duputel, and D. Helmberger (2014), The 2013, M_w 7.7 Balochistan earthquake, energetic strike-slip reactivation of a thrust fault, *Earth Planet. Sci. Lett.*, *391*, 128–134.

Bai, Y., and K. F. Cheung (2013a), Depth-integrated free surface flow with parameterized non-hydrostatic pressure, *Int. J. Numer. Methods Fluids*, *71*(4), 403–421.

Bai, Y., and K. F. Cheung (2013b), Dispersion and nonlinearity of multi-layer non-hydrostatic free-surface flow, *J. Fluid Mech.*, *726*, 226–260.

Bai, Y., K. F. Cheung, Y. Yamazaki, T. Lay, and L. Ye (2014), Tsunami surges around the Hawaiian Islands from the 1 April 2014 North Chile M_w 8.1 earthquake, *Geophys. Res. Lett.*, *41*, 8512–8521, doi:10.1002/2014GL061686.

Bilek, S. L., E. R. Engdahl, H. R. DeShon, and M. El Hariri (2011), The 25 October 2010 Sumatra tsunami earthquake: Slip in a slow patch, *Geophys. Res. Lett.*, *38*, L14306, doi:10.1029/2011GL047864.

Bletery, Q., A. Sladen, B. Delouis, M. Vallée, J.-M. Nocquet, L. Rolland, and J. Jiang (2014), A detailed source model for the M_w 9.0 Tohoku-Oki earthquake reconciling geodesy, seismology and tsunami records, *J. Geophys. Res. Solid Earth*, *119*, 7636–7653, doi:10.1002/2014JB011261.

Bürgmann, R., P. A. Rosen, and E. J. Fielding (2000), Synthetic aperture radar interferometry to measure Earth's surface topography and its deformation, *Annu. Rev. Earth Planet. Sci.*, *28*(1), 169–209.

Freymueller, J., N. E. King, and P. Segall (1994), The co-seismic slip distribution of the Landers earthquake, *Bull. Seismol. Soc. Am.*, *84*(3), 646–659.

Goldstein, R. M., H. Engelhardt, B. Kamb, and R. M. Frolich (1993), Satellite radar interferometry for monitoring ice sheet motion: Application to an Antarctic ice stream, *Science*, *262*, 1525–1530.

Hartzell, S. H., and T. H. Heaton (1983), Inversion of strong ground motion and teleseismic waveform data for the fault rupture history of the 1979 Imperial Valley, California, earthquake, *Bull. Seismol. Soc. Am.*, *73*(6A), 1553–1583.

Hill, E. M., et al. (2012), The 2010 M_w 7.8 Mentawai earthquake: Very shallow source of a rare tsunami earthquake determined from tsunami field survey and near-field GPS data, *J. Geophys. Res.*, *117*, B06402, doi:10.1029/2012JB009159.

Ji, C., D. J. Wald, and D. V. Helmberger (2002), Source description of the 1999 Hector Mine, California, Earthquake: Part I. Wavelet domain inversion theory and resolution analysis, *Bull. Seismol. Soc. Am.*, *92*(4), 1192–1207.

Johnson, J. M., K. Satake, S. R. Holdahl, and J. Sauber (1996), The 1964 Prince William Sound earthquake: Joint inversion of tsunami and geodetic data, *J. Geophys. Res.*, *101*(B1), 523–532, doi:10.1029/95JB02806.

Kaijura, K. (1963), The leading wave of a tsunami, *Bull. Earthquake Res. Inst.*, *41*, 535–571.

Kanamori, H. (2014), The diversity of large earthquakes and its implications for hazard mitigation, *Annu. Rev. Earth Planet. Sci.*, *42*, 7–26, doi:10.1146/annurev-earth-060313-055034.

Kikuchi, M., and H. Kanamori (1991), Inversion of complex body waves—III, *Bull. Seismol. Soc. Am.*, *81*(6), 2335–2350.

Kikuchi, M., H. Kanamori, and K. Satake (1993), Source complexity of the 1988 Armenian earthquake: Evidence for a slow after-slip event, *J. Geophys. Res.*, *98*(B9), 15,797–15,808, doi:10.1029/93JB01568.

Lay, T. (2014), The surge of great earthquakes from 2004 to 2014, *Earth Planet. Sci. Lett.*, *409*, 133–146.

Lay, T., C. J. Ammon, A. R. Hutko, and H. Kanamori (2010), Effects of kinematic constraints on teleseismic finite-source rupture inversions: Great Peruvian earthquakes of 23 June 2001 and 15 August 2007, *Bull. Seismol. Soc. Am.*, *100*, 969–994, doi:10.1785/0120090274.

Lay, T., C. J. Ammon, H. Kanamori, Y. Yamazaki, K. F. Cheung, and A. R. Hutko (2011a), The 25 October 2010 Mentawai tsunami earthquake (M_w 7.8) and the tsunami hazard presented by shallow megathrust ruptures, *Geophys. Res. Lett.*, *38*, L06302, doi:10.1029/2010GL046552.

Lay, T., Y. Yamazaki, C. J. Ammon, K. F. Cheung, and H. Kanamori (2011b), The 2011 M_w 9.0 off the Pacific coast of Tohoku Earthquake: Comparison of deep-water tsunami signals with finite-fault rupture model predictions, *Earth Planets Space*, *63*(7), 797–801, doi:10.5047/eps.2011.05.030.

Lay, T., L. Ye, H. Kanamori, Y. Yamazaki, K. F. Cheung, K. Kwong, and K. D. Koper (2013a), The October 28, 2012 M_w 7.8 Haida Gwaii underthrusting earthquake and tsunami: Slip partitioning along the Queen Charlotte Fault transpressional plate boundary, *Earth Planet. Sci. Lett.*, *375*, 57–70, doi:10.1016/j.epsl.2013.05.005.

Lay, T., L. Ye, H. Kanamori, Y. Yamazaki, K. F. Cheung, and C. J. Ammon (2013b), The February 6, 2013 M_w 8.0 Santa Cruz Islands earthquake and tsunami, *Tectonophysics*, *608*, 1109–1121, doi:10.1016/j.tecto.2013.07.001.

Lay, T., H. Yue, E. E. Brodsky, and C. An (2014), The 1 April 2014 Iquique, Chile, M_w 8.1 earthquake rupture sequence, *Geophys. Res. Lett.*, *41*, 3818–3825, doi:10.1002/2014GL060238.

Lorito, S., F. Romano, S. Atzori, X. Tong, A. Avalione, J. McCloskey, M. Cocco, and A. Piatanesi (2011), Limited overlap between the seismic gap and coseismic slip of the great 2010 Chile earthquake, *Nat. Geosci.*, *4*(3), 173–177, doi:10.1038/ngeo1073.

Massonnet, D., M. Rossi, C. Carmona, F. Adragna, G. Peltzer, K. Feigl, and T. Rabaute (1993), The displacement field of the Landers earthquake mapped by radar interferometry, *Nature*, *364*, 138–142.

Melgar, D., and Y. Bock (2013), Near-field tsunami models with rapid earthquake source inversions from land- and ocean-based observations: The potential for forecast and warning, *J. Geophys. Res. Solid Earth*, *118*, 5939–5955, doi:10.1002/2013JB010506.

Miyazaki, S., K. M. Larson, K. Choi, K. Hikima, K. Koketsu, P. Bodin, J. Haase, G. Emore, and A. Yamagiwa (2004), Modeling the rupture process of the 2003 September 25 Tokachi-Oki (Hokkaido) earthquake using 1 Hz GPS, *Geophys. Res. Lett.*, *31*, L21603, doi:10.1029/2004GL021457.

Newman, A. V., G. Hayes, Y. Wei, and J. Convers (2011), The 25 October 2010 Mentawai tsunami earthquake, from real-time discriminants, finite-fault rupture, and tsunami excitation, *Geophys. Res. Lett.*, *38*, L05302, doi:10.1029/2010GL046498.

Okada, Y. (1992), Internal deformation due to shear and tensile faults in a half-space, *Bull. Seismol. Soc. Am.*, *82*, 1018–1040.

Pollitz, F. F., R. Bürgmann, and P. Banerjee (2011), Geodetic slip model of the 2011 M9.0 Tohoku earthquake, *Geophys. Res. Lett*, *38*, L00G08, doi:10.1029/2011GL048632.

Romano, F., A. Piatanesi, S. Lorito, and K. Hirata (2010), Slip distribution of the 2003 Tokachi-oki M_w 8.1 earthquake from joint inversion of tsunami waveforms and geodetic data, *J. Geophys. Res.*, *115*, B11313, doi:10.1029/2009JB006665.

Romano, F., A. Piatanesi, S. Lorito, N. D'Agostino, K. Hirata, S. Atzori, Y. Yamazaki, and M. Cocco (2012), Clues from joint inversion of tsunami and geodetic data of the 2011 Tohoku-oki earthquake, *Sci. Rep.*, *2*, 385, doi:10.1038/srep00385.

Romano, F., E. Trasatti, S. Lorito, C. Piromallo, A. Piatanesi, Y. Ito, D. Zhao, K. Hirata, P. Lanucara, and M. Cocco (2014), Structural control on the Tohoku earthquake rupture process investigated by 3D FEM, tsunami and geodetic data, *Sci. Rep.*, *4*, 5631, doi:10.1038/srep05631.

Saito, T., Y. Ito, D. Inazu, and R. Hino (2011), Tsunami source of the 2011 Tohoku-Oki earthquake, Japan: Inversion analysis based on dispersive tsunami simulations, *Geophys. Res. Lett.*, *38*, L00G19, doi:10.1029/2011GL049089.

Satake, K. (1987), Inversion of tsunami waveforms for the estimation of a fault heterogeneity: Method and numerical experiments, *J. Phys. Earth*, *35*, 241–254.

Satake, K. (1989), Inversion of tsunami waveforms for the estimation of heterogeneous fault motion of large submarine earthquakes: The 1968 Tokachi-Oki and the 198e Japan Sea earthquakes, *J. Geophys. Res.*, *94*, 5627–5636, doi:10.1029/JB094iB05p05627.

Satake, K. (1993), Depth distribution of coseismic slip along the Nankai Trough, Japan, from joint inversion of geodetic and tsunami data, *J. Geophys. Res.*, *98*(B3), 4553–4565, doi:10.1029/92JB01553.

Satake, K., Y. Fujii, T. Harada, and Y. Namegaya (2013a), Time and space distribution of coseismic slip of the 2011 Tohoku earthquake as inferred from tsunami waveform data, *Bull. Seismol. Soc. Am.*, *103*(2B), 1473–1492.

Satake, K., et al. (2013b), Tsunami source of the 2010 Mentawai, Indonesia earthquake inferred from tsunami field survey and waveform modeling, *Pure Appl. Geophys.*, *170*, 1567–1582, doi:10.1007/s00024-012-0536-y.

Scholz, C. H. (1998), Earthquakes and friction laws, *Nature*, *391*, 37–42.

Shen, Z.-K., et al. (2009), Slip maxima at fault junctions and rupturing of barriers during the 2008 Wenchuan earthquake, *Nat. Geosci.*, *2*(10), 718–724.

Simons, M., and P. A. Rosen (2007), Interferometric synthetic aperture radar geodesy, in *Treatise on Geophysics–Geodesy*, vol. 3, pp. 391–446, Elsevier, Amsterdam.

Singh, S. C., N. Hananto, M. Mukti, H. Permana, Y. Djajadihardja, and H. Harjono (2011), Seismic images of the megathrust rupture during the 25th October 2010 Pagai earthquake, SW Sumatra: Frontal rupture and large tsunami, *Geophys. Res. Lett.*, *38*, L16313, doi:10.1029/2011GL048935.

Tanioka, Y., and K. Satake (1996), Tsunami generation by horizontal displacement of ocean bottom, *Geophys. Res. Lett.*, *23*, 861–864, doi:10.1029/96GL00736.

Tong, X., D. T. Sandwell, and Y. Fialko (2010), Coseismic slip model of the 2008 Wenchuan earthquake derived from joint inversion of interferometric synthetic aperture radar, GPS, and field data, *J. Geophys. Res.*, *115*, B04314, doi:10.1029/2009JB006625.

Tsai, V. C., J. P. Ampuero, H. Kanamori, and D. J. Stevenson (2013), Estimating the effect of Earth elasticity and variable water density on tsunami speeds, *Geophys. Res. Lett.*, *40*, 492–496, doi:10.1002/grl.50147.

Wang, R. (1999), A simple orthonormalization method for stable and efficient computation of Green's functions, *Bull. Seismol. Soc. Am.*, *89*, 733–741.

Wang, R., F. L. Martín, and F. Roth (2003), Computation of deformation induced by earthquakes in a multi-layered elastic crust—FORTRAN programs EDGRN/EDCMP, *C. R. Geosci.*, *29*, 195–207, doi:10.1016/S0098-3004(02)00111-5.

Watada, S., S. Kusumoto, and K. Satake (2014), Traveltime delay and initial phase reversal of distant tsunamis coupled with the self-gravitating elastic Earth, *J. Geophys. Res. Solid Earth*, *119*, 4287–4310, doi:10.1002/2013JB010841.

Yamazaki, Y., Z. Kowalik, and K. F. Cheung (2009), Depth-integrated, non-hydrostatic model for wave breaking and run-up, *Int. J. Numer. Methods Fluids*, *61*(5), 473–497.

Yamazaki, Y., K. F. Cheung, and Z. Kowalik (2011a), Depth-integrated, non-hydrostatic model with grid nesting for tsunami generation, propagation, and run-up, *Int. J. Numer. Methods Fluids*, *67*(12), 2081–2107.

Yamazaki, Y., T. Lay, K. F. Cheung, H. Yue, and H. Kanamori (2011b), Modeling near-field tsunami observations to improve finite-fault slip models for the 11 March 2011 Tohoku earthquake, *Geophys. Res. Lett.*, *38*, L00G15, doi:10.1029/2011GL049130.

Yamazaki, Y., K. F. Cheung, Z. Kowalik, G. Pawlak, and T. Lay (2012), NEOWAVE: Proceedings and results of the 2011 National Tsunami Hazard Mitigation Program (NTHMP) model benchmarking workshop, U.S. Department of Commerce NOAA NTHMP Special Report, pp. 239–302.

Yokota, Y., K. Koketsu, Y. Fujii, K. Satake, S. Sakai, M. Shinohara, and T. Kanazawa (2011), Joint inversion of strong motion, teleseismic, geodetic and tsunami datasets for the rupture process of the 2011 Tohoku earthquake, *Geophys. Res. Lett.*, *38*, L00G21, doi:10.1029/2011GL050098.

Yue, H., and T. Lay (2011), Inversion of high-rate (1 sps) GPS data for rupture process of the 11 March 2011 Tohoku earthquake (M_w 9.1), *Geophys. Res. Lett*, *38*, L00G09, doi:10.1029/2011GL048700.

Yue, H., and T. Lay (2013), Source rupture models for the 2011 Tohoku-Oki M_w 9.0 earthquake from joint inversions of high-rate geodetic and seismic data, *Bull. Seismol. Soc. Am.*, *103*, 1242–1255, doi:10.1785/0120120119.

Yue, H., T. Lay, S. Y. Schwartz, L. Rivera, M. Protti, T. H. Dixon, S. Owen, and A. V. Newman (2013), The 5 September 2012 Nicoya, Costa Rica M_w 7.6 earthquake rupture process from joint inversion of high-rate GPS, strong-motion, and teleseismic P wave data and its relationship to adjacent plate boundary interface properties, *J. Geophys. Res. Solid Earth*, *118*, 5453–5466, doi:10.1002/jgrb.50379.

Yue, H., T. Lay, L. Rivera, Y. Bai, Y. Yamazaki, K. F. Cheung, E. M. Hill, K. Sieh, W. Kongko, and A. Muhari (2014a), Rupture process of the 2010 M_w 7.8 Mentawai tsunami earthquake from joint inversion of near-field hr-GPS and teleseismic body wave recordings constrained by tsunami observations, *J. Geophys. Res. Solid Earth*, *119*, 5574–5593, doi:10.1002/2014JB011082.

Yue, H., T. Lay, L. Rivera, C. An, C. Vigny, X. Tong, and J. C. Baez Soto (2014b), Localized fault slip to the trench in the 2010 Maule, Chile M_w = 8.8 earthquake from joint inversion of high-rate GPS, teleseismic body waves, InSAR, campaign GPS, and tsunami observations, *J. Geophys. Res. Solid Earth*, *119*, 7786–7804, doi:10.1002/2014JB011340.

Zumberge, J. F., M. B. Heflin, D. C. Jefferson, M. M. Watkins, and F. H. Webb (1997), Precise point positioning for the efficient and robust analysis of GPS data from large networks, *J. Geophys. Res.*, *102*(B3), 5005–5017, doi:10.1029/96JB03860.